Joule

Article

Electrolyte design for aqueous Zn batteries

Graphical abstract

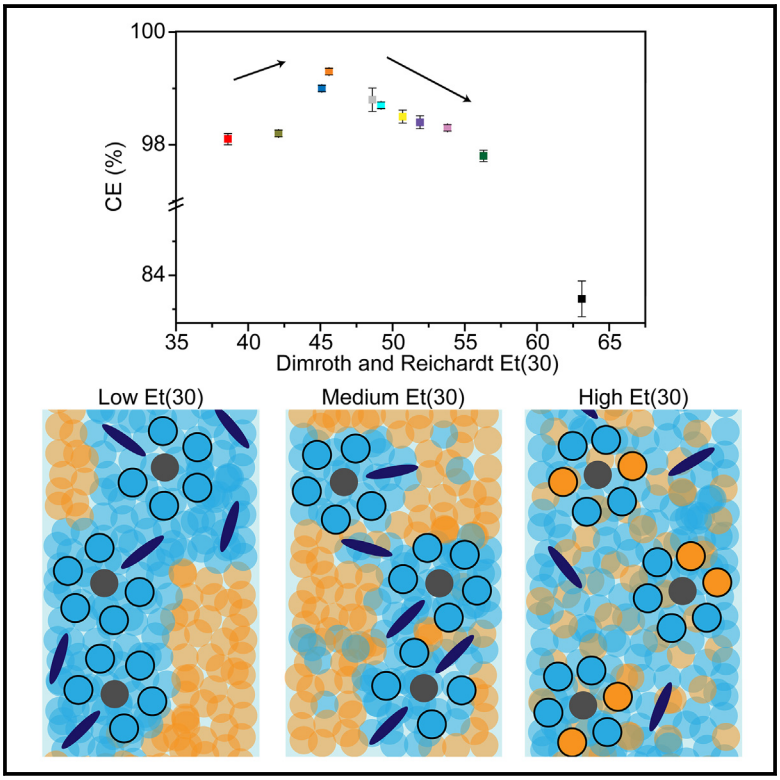

Highlights

- Thorough electrolyte design principles are suggested for aqueous batteries
- An effective descriptor for selecting organic co-solvent is discovered
- Designed electrolyte provides high reversibility and cycling stability of Zn batteries

Authors

Jiyun Heo, Dejian Dong, Zeyi Wang, Fu Chen, Chunsheng Wang

Correspondence

cswang@umd.edu

In brief

This study raises important questions about the effectiveness of traditional chemical properties as co-solvent selection descriptors and challenges prevailing assumptions about solvent polarity. We provide electrolyte design principles for aqueous batteries and introduce a powerful descriptor that demonstrates a clear correlation with battery performance. The electrolyte prepared based on the proposed guidelines enables the highly reversible and stable operation of zinc-based batteries by effectively suppressing side reactions and uncontrolled deposition of metal electrodes.

Heo et al., 2025, Joule 9, 101844
April 16, 2025
https://doi.org/10.1016/j.joule.2025.101844

CellPress

Joule

CellPress
OPEN ACCESS

Article

Electrolyte design for aqueous Zn batteries

Jiyun Heo,[1,3] Dejian Dong,[1] Zeyi Wang,[1] Fu Chen,[2] and Chunsheng Wang[1,4,*]
[1]Department of Chemical and Biomolecular Engineering, University of Maryland, College Park, MD 20742, USA
[2]Department of Chemistry and Biochemistry, University of Maryland, College Park, MD 20742, USA
[3]Present address: School of Chemical, Biological, and Battery Engineering, Gachon University, Seongnam-si, Gyeonggi-do 13120, Republic of Korea
[4]Lead contact
*Correspondence: cswang@umd.edu
https://doi.org/10.1016/j.joule.2025.101844

CONTEXT & SCALE Zn-based batteries with aqueous electrolytes are garnering great interest as the most promising next-generation batteries due to their intrinsic high safety, low cost, and environmental friendliness. However, the short cycle life of the Zn battery, originating from the low reversibility of the Zn metal electrode, is far from satisfactory. To achieve high reversibility of Zn metal electrode, tackling the water decomposition reaction and the inhomogeneous deposition/dissolution reaction is crucial. We present design principles for aqueous co-solvent electrolytes with high Zn reversibility and suggest a new parameter for accurately selecting beneficial organic molecules for Zn-based batteries. Electrolytes prepared using this principle effectively overcome the challenges in aqueous systems and demonstrate record-high cycling stability. This work provides new insight into aqueous electrolyte systems.

SUMMARY

Polarity scales are often used as descriptors for selecting organic molecules for aqueous Zn battery (AZB) electrolytes. However, failure to accurately predict the solvation of Zn^{2+} raises questions about their applicability for designing high-performance AZB electrolytes. Here, Dimroth and Richardt's Et(30) polarity scale is introduced as an effective guideline for screening organic molecules. A clear volcanic correlation is demonstrated between Et(30) and Zn Coulombic efficiency (CE). This challenges the common consensus in the aqueous electrolyte design formula, which typically uses highly polar organic molecules to improve Zn CE, and indicates that the roles of organic molecules beyond altering the Zn^{2+} solvation structure are critical for obtaining high AZB performances. Based on the Et(30) scale, the designed electrolyte achieves a high average Zn CE (99.8%), an exceptionally long cycle life (5,500 h), and a high specific energy (110 Wh kg^{-1}). Et(30) polarity scale offers general frameworks for selecting organic molecules in aqueous electrolytes.

INTRODUCTION

Aqueous Zn batteries (AZBs) have garnered significant interest due to their high energy density, safety, and low cost.[1] However, the lower potential of Zn redox reaction compared with water reduction induces hydrogen evolution reaction (HER) on the Zn electrode surface during Zn plating, resulting in low Coulombic efficiency (CE) of Zn plating/stripping.[2,3] In addition, the HER generates hydroxide anions, leading to the precipitation of Zn hydroxides on the Zn electrode, which promotes Zn dendrite growth and compromises cycling stability.[4]

HER during Zn plating is primarily driven by the reduction of solvating water in the Zn^{2+} cation shell, which can be pulled across the electric double layer.[5] The water coordinated with metal cations has a higher reduction potential than free water because the positive charge on metal cations makes the hydrogen in water molecules more reactive by strongly polarizing the coordinated water.[6] Therefore, reducing the water content in the Zn ion solvation shell is necessary to minimize water decomposition. Using organic co-solvents in aqueous electrolytes can effectively inhibit HER by decreasing the water coordination to the Zn ion.[7] Organic co-solvents with high polarity are typically preferred because they are believed to strongly interact with Zn^{2+} and disrupt the interaction between water molecules. In this regard, empirical polarity scales, such as the dielectric constant, dipole moment, and donor number, are often used for selecting organic co-solvent candidates.[8–11] However, organic solvents with high values on these scales do not necessarily guarantee high Zn electrode performance, and thereby, their applicability is yet debatable.[12] This is because conventional polarity parameters do not accurately (1) represent the microscale interaction within a solvation sheath of ions, (2) reflect the molecule's properties as a solvent, and (3) include information related to the structure properties (e.g., specific interactions

and decomposition products). Failure to rely on the traditional parameters for building electrolyte design principles hinders the development of AZB and requests an investigation of a new constructive property scale that involves all the necessary information for predicting the solvating process.

Considering that the charge transfer reaction happens at the interface of the Zn/electrolyte, the changes in the Zn^{2+} solvation structure near the Zn surface are equivalently important as the changes in the bulk electrolyte phase. Designing an electrolyte that can form a hydrophobic, dense solid electrolyte interphase (SEI) is thus helpful for suppressing HER because the Zn^{2+} solvation structure undergoes dramatic changes along the Zn^{2+} migration through SEI via the repulsion of H_2O.[13,14] The formation of ZnF_2-based SEIs is particularly advantageous because a ZnF_2-rich SEI can not only suppress HER but also inhibit Zn dendrite growth due to the superior hydrophobicity and zinc-phobicity of ZnF_2.[15] A ZnF_2-rich SEI can be achieved by increasing the concentration of F-rich salts, which allows a preferential reduction of F-anions.[16] However, high concentrations of electrolytes (such as in the case of water-in-salt electrolytes) reduce ionic conductivity and increase costs, limiting practical applications. Adding an F-rich additive is an effective alternative approach to promote the formation of ZnF_2 SEI without compromising these properties. Nevertheless, adopting F-rich additives in aqueous electrolytes faces challenges due to the low solubility of F-rich organic additives in these electrolytes and the lack of guidelines for selecting suitable molecules. In addition, the reduction of organic co-solvent and additives during SEI formation may also produce gas, destabilizing the formed SEI.[17,18] The potential formation of gas from the reduction of organic molecules has been overlooked by the aqueous battery community and should be an essential criterion for selecting co-solvents and additives in aqueous electrolytes.

In this paper, we present comprehensive criteria for selecting beneficial organic molecules for AZB electrolytes, which consider the proper polarity of organic molecules to ideally adjust the Zn^{2+} solvation shell, partitioning of water molecules between water-rich and organic-rich regions, gas generation from solvent decomposition, and effective SEI formation ability. While other frequently used traditional parameters cannot accurately reflect these considerations, the Et(30) polarity scale is discovered as an effective descriptor for designing high-performance AZB electrolytes. Interestingly, a clear volcanic relationship is demonstrated between Et(30) and Zn CE, with the maximum Zn CE occurring at Et(30) ~45. This challenges the common belief in the requirement of organic molecules' polarity and indicates that the guidelines for AZB electrolyte design should consider the roles of organic molecules beyond the interaction with Zn^{2+}. Guided by the proposed rules, the designed electrolyte achieves highly uniform Zn morphology with ZnF_2-rich SEI, a high CE of 99.8%, and allows a 25 μm-thin Zn anode to extend the cycle life to ~5,500 h with a record-high accumulative discharge capacity per theoretical Zn electrode capacity (190 mAh mAh_{Zn}^{-1}). Additionally, a polyaniline-based AZB (PANI-based AZB) using the designed electrolyte can stably operate under various conditions with a high specific energy density (~110 Wh kg^{-1}). We believe the newly proposed design rule and descriptor for organic molecule selection offer a powerful tool for building better batteries with aqueous electrolytes.

RESULTS AND DISCUSSION

Organic co-solvent selection

The organic co-solvent for AZB electrolytes must be soluble in aqueous electrolytes and capable of expanding the stability window of these electrolytes at low concentrations. We selected organic solvents based on their solubility in water (Table S1) and determined the minimum co-solvent quantity required to achieve a wide electrochemical stability window by measuring the stability window of 2 m LiTFSI/H_2O-solvent electrolytes using a three-electrode beaker cell configuration at a scan rate of 10 mV s^{-1} (Figure S1). The average Zn CEs over 100 cycles (except the AC and H_2O due to cell failure at approximately the 80^{th} and 40^{th} cycles, respectively) for each electrolyte were measured in Zn||Cu asymmetric cells using 1 m $Zn(TFSI)_2$/H_2O-solvent electrolytes (Figure S2). The average Zn CEs of the co-solvent electrolytes against the polarity parameters of the co-solvents are shown in Figure 1A. Commonly used polarity scales (dielectric constant, dipole moment, electrostatic factor, and donor number) did not exhibit a meaningful correlation with Zn CE, revealing the inapplicability of these scales for predicting Zn CE in co-solvent aqueous electrolytes. This is logical since these parameters do not fully reflect the requirements of co-solvents in aqueous Zn electrolytes. For example, the dielectric constant and dipole moment represent bulk solvent polarity properties (i.e., macroscale parameters) and often fail to correlate with ion solvation structures that occur on a microscale within a structured discontinuum of individual solvent molecules.[19] The electrostatic factor, a popular parameter used to explain solvent polarity, is derived by multiplying the dipole moment and dielectric constant; thus, it is also unsuitable for representing microscale solvent effects.[20] The donor number is a polarity index defined as the enthalpy of 1:1 adduct formation between $SbCl_5$ and target molecules diluted in an inert solvent system.[21] This makes the value more indicative of the polarity of the molecules as solutes rather than as solvents. Therefore, the donor number of solvents with strong cooperative effects varies significantly with their coordinating nature, and the donor number of mono-water is 18, while that of bulk water is 33.[22–24]

Et(30), Dimroth and Reichardt's polarity scale reflects both the polarity and hydrogen bonding capability (H_2O solubility and gas formation potential) of solvents.[19,25] It is an empirical parameter that measures the polarity of solvent molecules (including specific interactions like electron pair interaction and nonspecific interactions like Coulombic force) for general solvation ability, using dye molecules with solvatochromism properties. Et(30) effectively represents a molecule's polarity as a solvent because the dye molecules are completely solvated by the target molecule of interest. Additionally, Et(30) strongly correlates with the hydrogen bonding ability of solvents. Solvents with Et(30) < 40 are classified as aprotic nonpolar solvents, those with Et(30) between 40 and 47 as aprotic polar solvents, and those with Et(30) > 47 as protic polar solvents. Consequently, Et(30) shows a good repeatable correlation with the CE of Zn. This indicates the potential of Et(30) as a descriptor for exploring co-solvents for AZBs, covering a broad range of chemical information that other chemical properties cannot deal with, although there is little expense of specificity (Note S1). It is important to note that

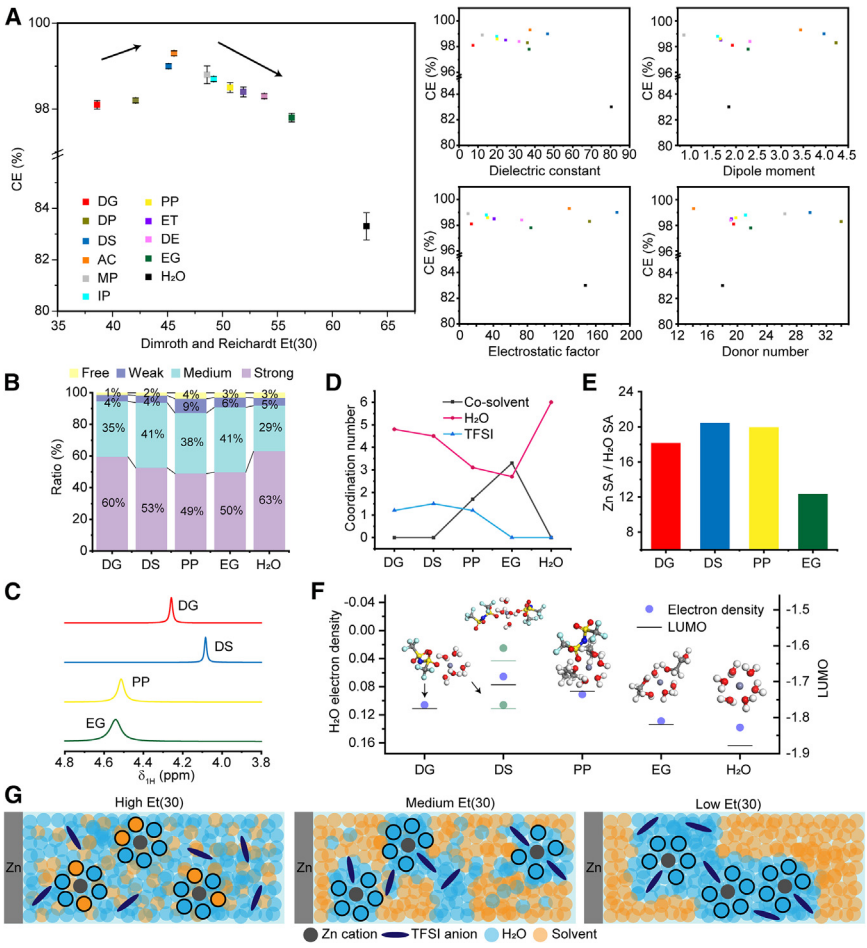

Figure 1. Et(30) parameter for co-solvent electrolyte design

(A) Relationship between Zn CE and the polarity scales of various solvents.

(B) Ratio of hydrogen bonding networks in different electrolytes obtained from attenuated total reflection-Fourier transform infrared (ATR FTIR) analysis.

(C) ^{1}H nuclear magnetic resonance (NMR) spectra of each electrolyte.

(D–F) Computational analysis of co-solvent electrolytes: (D) Zn^{2+} coordination number with solvents, water, and TFSI anion; (E) Zn^{2+} and H_2O solvation affinity (SA) ratio in pure solvents; and (F) comparison of H_2O electron density and lowest unoccupied molecular orbital (LUMO) of 1st solvation cluster.

(G) Schematic illustration depicting the variation in solvation structure with Et(30) values.

while higher solvent polarity is generally considered beneficial for improving CE,[7,26] there is an optimal Et(30) range that results in the highest reversibility of the Zn redox reaction, as demonstrated by the volcanic relationship between Et(30) and CE. This is because a solvent with too low Et(30) cannot effectively suppress H_2O activity due to weak interactions with either water or Zn^{2+}, while a solvent with too high Et(30) cannot reduce the polarization of Zn-solvating water as it prevents anion entrance into Zn ion's 1st solvation shell and may produce gas leading to low Zn CE. This volcanic relationship between Zn CE and Et(30), as well as the irregular relationship between Zn CE and other polarity scales, also holds at the 200th cycle (Figure S3), and with the Et(30) of aqueous/nonaqueous mixture solvent (Figure S4).[27,28] The polarity parameters of each solvent used for comparison are provided in Table S1.

Solvation structure of aqueous electrolyte with organic solvent

To investigate the fundamental reason for this phenomenon, the hydrogen bond (HB) networks of five representative electrolytes in different categories (nonpolar aprotic [DG], protic [DS], and polar protic [PP and EG] organic co-solvent electrolytes) were analyzed using attenuated total reflection-Fourier transform infrared (ATR FTIR) spectroscopy, as shown in Figures 1B and S5. From Table S1, the Et(30) values increased in the order of DG (38), DS (45.1), PP (50.7), EG (56.3), and H_2O (63.1). For solvents in the high Et(30) range (H_2O to PP; 63–50), there was a gradual decrease in HBs within the electrolyte as Et(30) decreased due to the reduced HB-forming affinity along the series of solvents. However, despite the lower HB-forming ability in the PP to DG range, strong HBs in the electrolytes indicate recovery of interactions between water molecules (Figure 1B). This finding aligns with previous studies on the hydrophobic solvation of aprotic solvents, where lower Et(30) corresponds to higher hydrophobicity, thereby enhancing interactions between water molecules.[29,30] Electron density variation in water molecules was verified using ^{1}H nuclear magnetic resonance (NMR) to gain further insight into the changes in the chemical environments of water (Figure 1C). A general trend of increasing electron density with decreasing Et(30) was observed. This can be understood in terms of the strong correlation between HB donating ability and Et(30), and since EG has the highest HB donating ability, it can most effectively reduce the electron density of protons in water molecules, whereas this effect is weakest for the solvent with the lowest Et(30), DG. The DS electrolyte appears to be an outlier, indicating the presence of a factor beyond the solvent's effect on water electron density. Considering the DS electrolyte's deviation toward higher electron density, the additional factor likely involves the contribution of the anion.

The computational calculations offer deeper insights into the volcanic relationship between Et(30) and the reversibility of Zn. The changes in Zn ion's 1st solvation structure using different co-solvents were observed from radial distribution functions (RDFs, Figures 1D and S6). In electrolytes with high Et(30) solvents (i.e., highly polar solvents), the 1st solvation shell of the Zn ion was occupied by water and solvent molecules. When mid- to low-Et(30) solvents were used as co-solvents, the TFSI anion began participating in the solvation structure, reaching a

maximum TFSI coordination number in the DS electrolyte. These results match well with the peak shifts in TFSI anion's peaks in FTIR analyses (Figure S7).[31] The lower TFSI coordination number observed in the DG electrolyte compared with the DS electrolyte can be understood from the water distribution in the electrolyte. As shown in Figure S8, the uniformity of water distribution decreased with the Et(30) value, and H_2O was uniformly distributed in the electrolyte for EG and PP, while water was trapped in the water-rich zone for DG. Although the DS electrolyte also formed a water-rich zone, some water molecules were freely coordinated with the DS molecule due to DMSO's higher polarity than diglyme. These results align with the FTIR and ^{1}H NMR findings, and the formation of water-rich zones in DS and DG electrolytes explains the increase in strong HB observed in FTIR spectra, while the highest TFSI coordination number provides clues for the highest electron density of water in the DS electrolyte, as seen in ^{1}H NMR results. To numerically explain the changes in the solvation structure, the affinity of Zn solvation and water solvation in pure water to each solvent were compared in Figure S9, and the ratios of solvation affinity (SA) are provided in Figure 1E. The DS electrolyte exhibits the highest value, indicating that the Zn cation is more likely to be solvated by water than by DMSO, while the water molecule can dissolve in both water and DMSO due to the moderate solvation capability of DMSO. This leads to the formation of a high-concentration, water-rich zone in the DS electrolyte with high Zn-TFSI coordination, as supported by the RDF results. Some studies suggest that DMSO can occupy the 1st solvation shell of Zn ions in aqueous electrolytes based on traditional polarity scales, such as dielectric constant and donor number.[32] Consequently, we examined the bond structure changes in DMSO with Zn salt dissolution. As shown in Figures S10A and S10B, the peak positions related to the oxygen bonds shift to those characteristics of pure DMSO when Zn salt is added to the solvent mixture (DS4H1). This occurs because Zn ions require the exclusion of water from the coordination environment with DMSO for the Zn cation solvation process. Consequently, the presence of water decreases in the DMSO-rich region, making it resemble the pure DMSO state. This differs from co-solvent with high Et(30) in that dissolving Zn salt does not shift back the peak for the organic solvent to its pure state.[8] Similar findings were observed for Li solvation in the DMSO/water mixture and acetonitrile/water mixture,[33,34] highlighting the unsuitability of using high donor concepts to predict cation solvation structures in the electrolyte (at least true for the aqueous solvent system). Furthermore, the poor solvation of DMSO compared with H_2O is indirectly evidenced by the solubility of Zn salt (Figure S10C). The failure of traditional polarity scales to predict Zn ion solvation in solvents is consistent with other reported findings.[21,35,36]

Changes in the 1st solvation structure are directly related to the reversibility of the Zn redox reaction. This is because water molecules in the 1st solvation shell readily participate in the HER by losing electrons to the Zn cation, which weakens the bond between O and H.[37,38] Figure 1F illustrates the average electron density of H_2O in each solvation scheme. The DS electrolyte, with a 1.5 coordination number of TFSI, used an average electron density of two TFSI and one TFSI solvation scheme (marked in blue) for comparison. A strong correlation was observed between Zn reversibility and H_2O electron density, with the highest H_2O electron density found in the DS electrolyte, aligning with the highest CE of the Zn reaction. The lowest unoccupied molecular orbital (LUMO) level of each electrolyte followed a similar trend, displaying a volcanic correlation with the DS electrolyte having the highest LUMO. These findings indicate that reducing water polarization in the Zn solvation shell is crucial for minimizing the side reactions of water. Moreover, anion coordination, rather than organic co-solvent coordination, is more effective in stabilizing water within the Zn solvation shell.

It is important to note that solvents with high Et(30) values are protic solvents that generate a gas product (H_2) during the solvent reduction reaction.[39–41] As mentioned above, high Et(30) solvents are incorporated into the Zn solvation shell, making them susceptible to reduction reactions. Gas generation can destabilize the formed SEI, potentially leading to the low CE observed in electrolytes with high Et(30) solvents. Our findings challenge the common belief that higher polarity solvents improve Zn CE, instead highlighting the need to consider the competition between solvents and anions for Zn ion coordination and the products of solvent reduction.

The schematic illustration in Figure 1G depicts changes in the solvation structure of Zn ions in co-solvent aqueous electrolytes with varying Et(30) values. When a protic polar solvent with high Et(30) is used, the Zn ion can be solvated by both water and the protic polar solvent, leading to gas generation upon reduction of the solvent molecules, which reduces Zn CE. In addition, the high-polarity protic solvent inhibits anion entry into the 1st solvation shell of the Zn ion, resulting in low Zn CE due to insufficient stabilization of H_2O. In an electrolyte with a low Et(30) solvent, water molecules primarily solvate the Zn ion in a water-rich region due to the organic solvent's low polarity. In such water-rich regions, few anions enter the 1st solvation shell of the Zn ion. For electrolytes using an aprotic polar solvent with a mid-range Et(30), water can form a water-rich zone while coordinating with the organic solvent due to the optimal polarity of the organic solvent, reducing the water concentration in the water-rich zone. Combined with the gas-free reduction of an aprotic polar solvent, favorable anion occupation in Zn's 1st solvation shell results in a high Zn CE.

F-containing additives selection

Although the aqueous electrolyte with the DS co-solvent (DSZT) achieved the highest Zn CE among the solvents investigated, this Zn CE remains relatively low. Forming an F-rich SEI on Zn via the reduction of TFSI anions is challenging due to the high redox potential of Zn/Zn^{2+}. F-rich SEI can also be formed through the reduction of F-containing additives in water, but the low solubility of these additives in water limits their effectiveness. Adding an organic co-solvent to aqueous electrolytes makes it possible to introduce water-insoluble F-containing additives into the co-solvent electrolytes (Figure S11).

The physical and chemical properties (such as donor number and Et(30)) of specific molecules are often elusive in databases, particularly for uncommon molecules derived from conventional organic molecules (i.e., parent molecules) modified with specific functional groups such as $-CF_3$. Consequently, rational selection of specific additives is challenging. Given that the

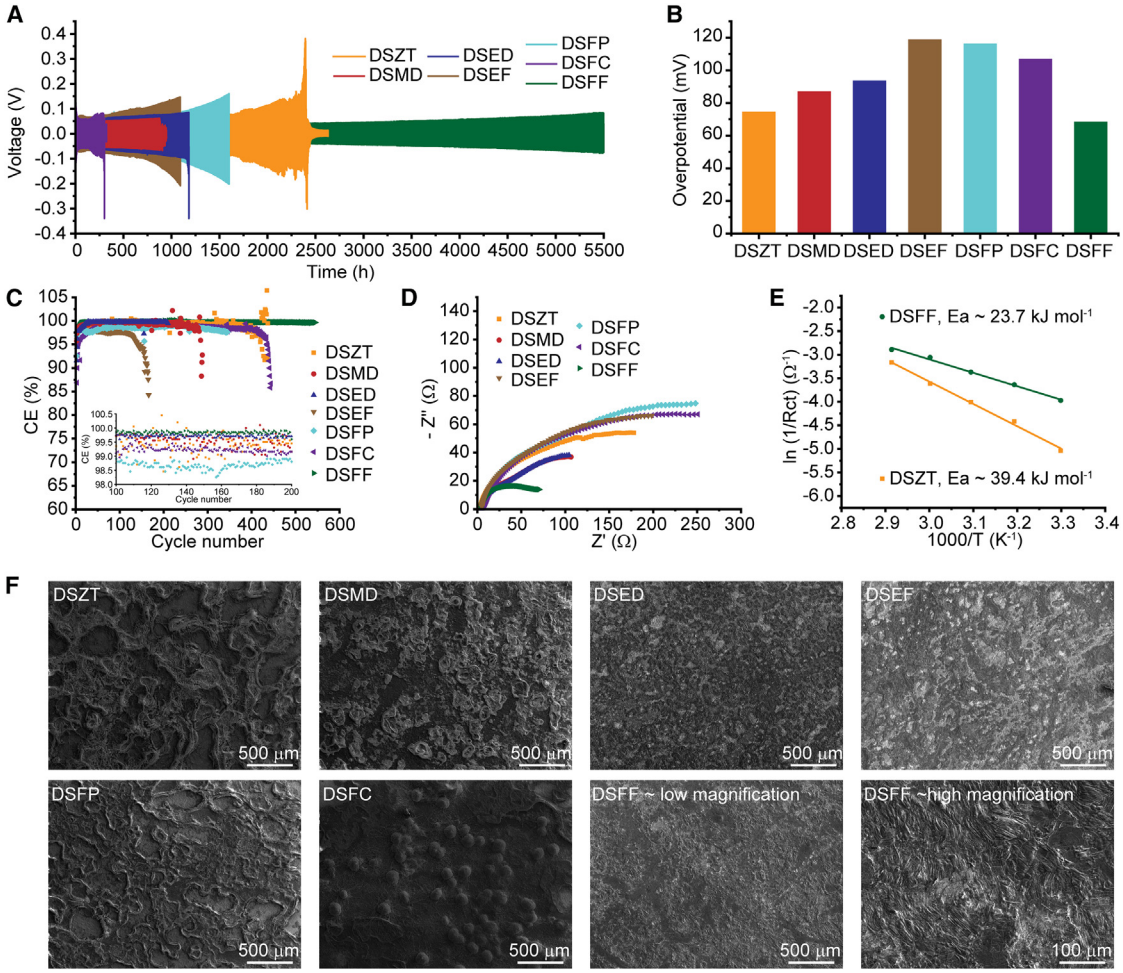

Figure 2. Performance evaluation of electrolytes with 0.5 m F-based additives

(A) Cycle life comparison using Zn||Zn symmetric cells under 1 mA cm^{-2} and 1 mAh cm^{-2} operating condition.

(B) Overpotential at the 50th cycle for each cell using different electrolytes.

(C) CE of Zn plating/stripping measured using Zn||Cu asymmetric cells under 1 mA cm^{-2} and 1 mAh cm^{-2} conditions.

(D) Electrochemical impedance spectroscopy (EIS) of Zn||Zn cells with different electrolytes.

(E) Activation energy of the charge transfer reaction derived from EIS spectra at various temperatures (30°C–70°C).

(F) Surface scanning electron microscopy (SEM) images of Zn electrodes cycled in each electrolyte (10 cycles, 1 mA cm^{-2}, 1 mAh cm^{-2}).

Et(30) values of the parent molecules can be found, and the specific molecule with minor functional group modifications should have a similar Et(30) to the parent molecule,[42] we select additives based on the Et(30) of the parent molecules. To validate the universality of Et(30), we selected several F-containing additives where the Et(30) of the parent molecules ranged from 38 to 49 (Figure S12), as co-solvents within this range showed great performance in aqueous electrolytes (Figure 1). Among the candidates, molecules without –OH bonds were selected to prevent gas formation that could destabilize the SEI layer. The toxicity, flammability, and water reactivity of these molecules were also considered to ensure the safety of the aqueous electrolyte. Based on these criteria, methyl difluoroacetate (MD), ethyl difluoroacetate (ED), ethyl trifluoroacetoacetate (EF), trifluoro pentanedione (FP), fluoroethylene carbonate (FC), and trifluoroethyl formate (FF) were selected at a concentration of 0.5 m as additive candidates for DS electrolytes (DSZT), forming DSMD, DSED, DSEF, DSFP, DSFC, and DSFF electrolytes. The cycle life of Zn||Zn (25 μm Zn) symmetric cells with these additives was evaluated first. The additive-containing electrolytes did not necessarily extend the cycle life or reduce the overpotential compared with the reference DSZT electrolyte. However, the DSFF electrolyte improved both cycling stability and reaction kinetics (Figures 2A, 2B, and S13). The cycle life of the Zn electrode in the DSFF electrolyte is compared with previously reported Zn electrodes in Table S2. Most reported studies did not achieve half of our result when considering the thickness of the Zn electrode. Further comparisons of cycling performance between DSFF (with FF additive) and DSZT (without additive) electrolytes under various current densities with a fixed step time (1 h for each charge and discharge step, Figure S14) showed

that the FF additive significantly improved cycling stability, even under harsh conditions of 3 mA cm^{-2} and 3 mAh cm^{-2}.

The Zn CE with different electrolytes was also measured using a Zn||Cu asymmetric cell configuration (Figure 2C). Consistent with the cycling stability test results, DSFF exhibited the highest average CE of 99.8% over 550 cycles, whereas other electrolytes showed little improvement (or even decrease) in CE compared with the DSZT electrolyte (99.3%). This outcome demonstrates the FF additive's superiority in improving the performance of Zn electrodes regarding both cycling stability and reversibility, which is likely related to its regulation effect on the solvation structure of Zn ion (Figure S15; Note S2). One thing that should be mentioned is the differences in cycling stability of Zn||Zn asymmetric cell and Zn||Cu asymmetric cell are quite often observed, as noted from previous papers.[43–45] While electrodeposition is governed by countless factors (e.g., solvation structure of metal ions and side reactions), the interaction between metal adatom and the substrate is typically used for explaining such a tendency.[46] When plotting the CEs of electrolytes against the polarity scales of each additive's parent molecules, a volcanic correlation was observed for Et(30), while other polar scales showed random distribution (Figure S16). The parent molecules with Et(30) values between 40 and 45 achieved the highest Zn CE, similar to the results from solvent selection. Although the mechanism behind this correlation remains unclear due to the complex quinary interactions between components, our results indicate the potential use of Et(30) for selecting co-solvent and additives. The high reversibility of the Zn reaction with DSFF electrolyte was further confirmed under conditions of 3 mA cm^{-2} and 3 mAh cm^{-2} (Figure S17). Again, DSFF electrolytes demonstrated better reversibility than DSZT electrolytes (99.7% for DSFF and 97.7% for DSZT), as the formation of an F-based SEI suppressed the water decomposition reaction (discussed in the following section). The Zn CE and overpotential measured using the reservoir method also confirmed the improved reversibility of the Zn redox reaction by FF addition into the electrolyte (Figure S18).

The effectiveness of the FF additive in improving the Zn reversibility was also verified in other different co-solvents. As shown in Figure S19, the addition of FF additive into the co-solvent electrolytes could notably improve the Zn CE. The FF additive especially greatly improved Zn performance with high Et(30) solvents (PP and EG). Since high Et(30) solvents are found to have a weaker effect on HER suppression, this can be rationally understood by further suppression of HER due to the strong hydrophobicity of F-based SEI.

The electrochemical impedance spectroscopy (EIS) of Zn||Zn cells in various electrolytes was measured (Figure 2D). The inclusion of additives generally reduced ionic conductivity due to a slight increase in viscosity, as the additives are somewhat bulky (Figure S20). However, using FF significantly reduced the charge transfer resistance (R_{ct}), consistent with the lowest overpotential shown in Figure 2B. The activation energy of the Zn redox reaction in DSZT and DSFF electrolytes was calculated from the R_{ct} over a temperature range of 30°C–70°C (Figures 2E and S21). The FF additive decreased the activation energy of the charge transfer reaction by 40%, confirming its effectiveness in improving the Zn redox reaction performance.

The morphologies of cycled Zn electrodes in each electrolyte were compared using surface scanning electron microscopy (SEM, Figures 2F and S22). The Zn electrode in the DSFC electrolyte exhibited a nonuniform morphology with large boulder-like Zn deposits. Zn electrodes from DSZT, DSMD, and DSFP electrolytes showed similar mountain range-like surfaces with varying degrees of nonuniformity (DSZT > DSFP > DSMD). Flat and uniform surface morphologies were observed in Zn electrodes from DSED, DSEF, and DSFF electrolytes. However, Zn electrodes from DSED and DSEF showed heterogeneous small boulder-like Zn deposits at higher magnifications (Figure S23), whereas the DSFF sample exhibited a highly uniform surface morphology with clear lattice growth.

Additive-derived SEI

The formation of the SEI in DSFF electrolytes was validated by deviations in sweep voltammetry Zn plating curves. The dI/dV curve revealed an additional reduction peak for the DSFF electrolyte compared with the reference DSZT electrolyte (Figure 3A). This indicates that the FF additive can be reduced before the Zn redox reaction, as suggested by the low LUMO level (Note S2), likely leading to stable SEI formation by the FF. Surface analysis of the Zn electrodes cycled in DSFF electrolyte using X-ray photoelectron spectroscopy (XPS) confirmed the SEI layer formation. The Zn electrode cycled with DSZT electrolyte showed mostly solvent reduction peaks (Figure 3B), whereas clear peaks for F-containing components were observed on the Zn electrode cycled with DSFF (Figure 3C). This confirms the successful formation of ZnF_2 SEI by the FF additive. As previously mentioned, the formation of ZnF_2-rich SEI is significant due to its high hydrophobicity and zinc-phobicity. The hydrophobic property of ZnF_2 can block water penetration, while its zinc-phobic property can suppress Zn dendrite growth.[47] Therefore, the improved performance of the Zn electrode with the DSFF electrolyte is closely related to the formation of ZnF_2-rich SEI layers. Additionally, a thin layer of ZnS was formed outside of ZnF_2 for the Zn electrode cycled with DSFF electrolytes, but it was absent near the Zn electrode surface. Since the ZnS outer layer has high mechanical strength and ionic conductivity, and the ZnF_2 inner layer suppresses Zn dendrite growth with low overpotential,[48] the DSFF electrolyte could outperform other tested electrolytes.

In DSZT electrolytes, a significant peak associated with oxygen vacancies in ZnO was observed in the O1s XPS spectra on the surface of the cycled Zn electrode (Figure S24).[49] Since oxygen vacancies in ZnO are active catalytic sites for the HER,[50,51] the degree of H_2 gas generation was compared for DSZT and DSFF electrolytes during cycling. As shown in Figure 3D, more H_2 gas was produced throughout the cycling process for the DSZT electrolyte, with occasional spikes due to H_2 bubble detachment. This is likely because the hydrophobic ZnF_2-based SEI is absent, and there are abundant oxygen vacancies in ZnO for the Zn electrode cycled with DSZT electrolyte. To further verify the effect of SEI layers, pressure development tests were conducted using Zn electrodes pre-cycled in DSZT and DSFF electrolytes (Figure S25). Similar results could be obtained with Figure 3D, although the same DSZT electrolyte was utilized during the test. This clearly explains the effect of the hydrophobicity of SEI on suppressing HER. During operation in

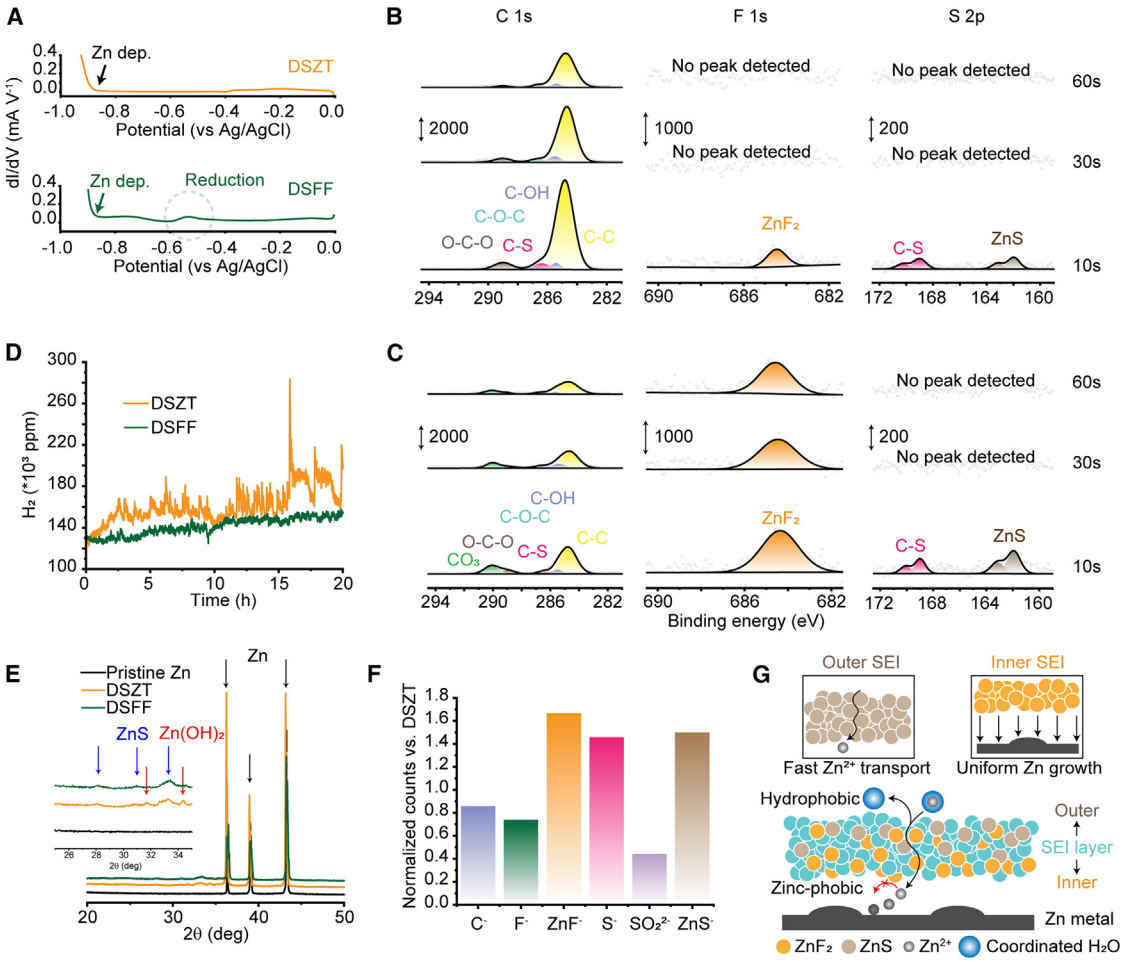

Figure 3. F-based SEI formation from FF additive reduction

(A) dI/dV curve of DSZT and DSFF electrolytes (scan rate: 10 mV s^{-1}).

(B and C) X-ray photoelectron spectroscopy (XPS) spectra of Zn electrodes cycled in (B) DSZT and (C) DSFF electrolytes, displaying C 1s, F 1s, and S 2p regions (from left to right).

(D) *In situ* H_2 evolution detection using gas chromatography (20 h cycle at 1 mA cm^{-2} and 1 mAh cm^{-2}).

(E) X-ray powder diffraction (XRD) analysis of Zn electrode surfaces.

(F) Time-of-flight secondary ion mass spectrometry (ToF-SIMS) intensity comparison of various species on Zn electrodes cycled in DSZT and DSFF electrolytes.

(G) Beneficial ZnF_2/ZnS SEI structure on Zn metal surface cycled in DSFF electrolyte. All samples for post-mortem analyses were obtained after one cycle under 1 mA cm^{-2} and 1 mAh cm^{-2} conditions.

AZBs, HER can significantly affect the performance of the Zn electrode. This occurs because HER consumes electrons, reducing the CE of the Zn redox reaction, and leads to the formation of Zn hydroxide species, causing uneven Zn growth.[52] Figure 3E shows the X-ray powder diffraction (XRD) spectra of the Zn electrode after cycling in DSZT and DSFF electrolytes. The formation of crystalline $Zn(OH)_2$ on the Zn electrode from DSZT indicates a higher degree of HER for the DSZT electrolyte than DSFF, consistent with the gas chromatography results.

A time-of-flight secondary ion mass spectrometry (ToF-SIMS) analysis was also conducted to verify the SEI components on the Zn electrode (Figure 3F). The results were consistent with those from XPS. The ZnF^- signal intensity on Zn with the DSFF electrolyte was much higher than in DSZT due to the formation of ZnF_2 SEI in DSFF, while the F^- signal was lower than in the DSZT sample, indicating a higher degree of F-species reduction with DSFF. In addition, the ZnS^- signal in DSFF was 40% higher than in DSZT. These findings confirm the successful formation of dual F/S-based SEI in the DSFF electrolyte (Figure 3G). ToF-SIMS spectra of each component are provided in Figure S26.

Zn||PANI full-cell performance

The performance of the DSFF electrolyte was evaluated using Zn||PANI full cells and compared with the same cells with the DSZT electrolyte. The Zn||PANI full cell with DSFF electrolyte demonstrated a higher specific capacity (130 mAh g^{-1}, approximately 0.5 mAh cm^{-2}) and longer cycle stability (1,000 cycles) than the capacity (90 mAh g^{-1}) and cycle stability (300 cycles)

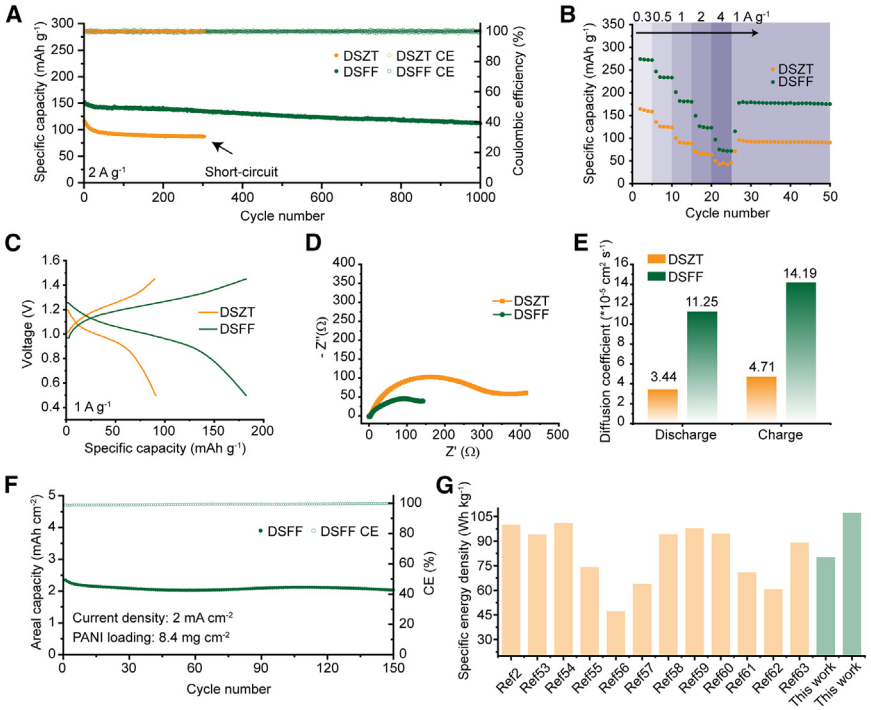

Figure 4. Zn||PANI full-cell performance improvement using the designed electrolyte

(A) Comparison of long-term cycling performance at 2 A g^{-1}.

(B) Rate capability test across a current density range of 0.3–4 A g^{-1}.

(C) Voltage profiles of Zn||PANI full cell at 1 A g^{-1}.

(D) Nyquist plot from impedance analysis.

(E) Diffusivity of Zn ions in each electrolyte.

(F) Performance of pouch-type AZB using DSFF electrolyte.

(G) Specific energy density comparison with previous studies. All specific current densities are calculated based on the weight of PANI.

achieved with DSZT electrolyte (Figure 4A). The DSZT full cell showed rapid capacity decay at the early stage of the charge/discharge process and short-circuited at 300th cycles. By contrast, the DSFF full cell maintained high capacity and capacity retention due to the formation of a ZnF_2-rich SEI. Increasing the PANI loading to 1.1 mAh cm^{-2}, the Zn||PANI cell with DSFF electrolyte again demonstrated longer cycling stability compared with DSZT electrolytes (Figure S27), confirming the importance of Zn metal stability for overall AZB performance.

The Zn||PANI cell with DSFF electrolytes also exhibited higher rate capability than DSZT electrolytes. As shown in Figure 4B, the Zn||PANI cell with DSFF electrolyte showed higher capacity across all current densities (0.3–4 A g^{-1}) than the DSZT electrolyte. The voltage profile comparison (Figures 4C and S28) revealed a clear improvement in overpotential and capacity with the addition of the FF additive. This correlated with the lower resistance of the Zn||PANI cell using DSFF electrolyte compared with DSZT (Figure 4D). The performance enhancement by the DSFF electrolyte likely originated from the fast mass transport of Zn ions near the PANI cathode (Figures 4E and S29).

The benefits of using the DSFF electrolyte in full-cell performance were further examined under harsh conditions. For practical application, AZBs require a large areal capacity for high energy density. Therefore, a pouch-type AZB with a PANI cathode having a high loading of 8.4 mg cm^{-2} (440 μm thickness, Figure S30) was evaluated with DSFF electrolytes. These pouch-type Zn||PANI cells operated for over 150 cycles with an average areal capacity of 2.1 mAh cm^{-2} (Figure 4F). Increasing the PANI capacity to 3.7 mAh cm^{-2} was also successful, achieving a high specific energy density (107.3 Wh kg^{-1} based on the weight of PANI and Zn, Table S3) using a 25 μm Zn electrode, as shown in Figure S31, outperforming previous reports (Figure 4G).[2,53–63] Additionally, the performance of Zn||PANI cells was evaluated at different temperatures. The DSZT full cell failed quickly at a high temperature (4°C, Figure S32) due to nonuniform Zn growth. However, the DSFF full cell showed stable operation owing to the protective F-based SEI on the Zn electrode, which regulated Zn deposition morphology. Performance differences between the two electrolytes were even more pronounced at low temperatures (0°C). The Zn||PANI full cell with DSZT could not operate due to high overpotential (Figure S33) from low mass transport kinetics, while the cell with DSFF functioned stably for over 350 cycles with a reasonably high specific capacity (~120 mAh g^{-1}). Finally, Zn||PANI cells with DSFF electrolyte operated stably across −10°C to 60°C (Figure S34). These findings highlight the potential application of the newly designed electrolyte for high-performance AZBs.

Conclusions

We demonstrated that Dimroth and Reichardt's Et(30) is an effective descriptor for selecting organic molecules for AZB electrolytes. Contrary to the common belief that higher polarity of an organic molecule ensures higher CE, we found that an optimum Et(30) value around 45 yielded the highest Zn CE. This volcanic correlation is due to an optimum polarity range for organic molecules, which can create a high-concentration, water-rich zone, thereby altering the solvation structure of Zn ions to be primarily occupied by anions and minimizing water activity, with minimal solvent decomposition forming gas. Et(30) is a universal descriptor that can also be used to select additives, with the Et(30) of the additive's parent molecule showing a similar volcanic relationship with Zn CE. Following our design principle, the newly designed DSFF electrolyte exhibited high CE and remarkably stable Zn cycle life. Additionally, PANI-AZB with DSFF electrolytes demonstrated significantly better rate capability and higher capacity than the reference electrolytes. We believe this work provides valuable insights for future studies in related fields.

METHODS

Electrolyte preparation

Co-solvent organic-aqueous electrolytes were prepared by mixing organic solvents and water in varying weight ratios (XXnHm in Figure S1 indicates XX [organic solvent]:H (H_2O) = n:m by weight) using 2 m LiTFSI for the potential window test and 1 m $Zn(TFSI)_2$ for other experiments. The optimal organic solvent/water ratio was determined from the potential window test, and the sample with the widest potential window that did not further expand with more organic solvent was selected as the optimal ratio. For electrolytes with additives, 0.5 m of each candidate additive was added to the DSZT electrolyte (DS4H1 + 1 m $Zn(TFSI)_2$) based on the combined weight of the organic solvent and water.

Electrochemical analyses

All electrochemical tests were performed using 2032 standard coin cells, except the potential window and gas chromatography tests, which used a three-electrode beaker cell and a specific custom cell kit, respectively. The Zn||Zn symmetric cell was assembled using two Zn metal electrodes (thickness: 25 μm, diameter: 16 mm) separated by a glass fiber membrane (thickness: 0.42 mm, diameter: 19 mm). The Zn||Cu asymmetric cell was prepared similarly, with one Zn metal electrode replaced by a Cu metal electrode. For the three-electrode beaker cell, an Ag/AgCl (saturated KCl) electrode served as the reference, and 0.5 cm^2 Ti metal/Al metal was used for the working (counter)/counter (working) electrode in the anodic (cathodic) stability test. The gas chromatography test cell was configured the same way as the Zn||Zn symmetric cell. Unless mentioned, all the cells are operated at room temperature.

Galvanostatic experiments were conducted using the Landt battery test system. The specific current density and areal capacity conditions are detailed for each test. The CE test was conducted with a voltage cutoff of 0.5 V. The reservoir method followed a modified Aurbach protocol: (1) formation cycle at 1 mA cm^{-2} and 2 mAh cm^{-2}, (2) a reservoir Zn plating on Cu at 1 mA cm^{-2} and 2 mAh cm^{-2}, (3) cycling at 1 mA cm^{-2} and 0.2 mAh cm^{-2} for 300 cycles, and (4) stripping remaining Zn on Cu at 1 mA cm^{-2} until the 0.5 V voltage cutoff. The cycling test for *in situ* gas chromatography was conducted using a Gamry Instrument. All other electrochemical measurements were performed using a Biologic VSP electrochemical workstation. EIS data were collected over a frequency range of 0.1–10^6 Hz. Each linear sweep voltammetry (LSV) test was conducted at a scan rate of 10 mV s^{-1}.

PANI slurry was prepared by mixing commercial PANI powder (60 wt %), carbon nanotube (30 wt %), and polytetrafluoroethylene (PTFE, 10 wt %) in water and ethanol. After drying in an 80°C oven for at least 12 h, the PANI cathode was pressed onto an activated carbon cloth substrate. The PANI cathode was cut into 9 mm disks for coin cell tests, with a PANI loading of 3.5–4.5 mg cm^{-2}, except for the high-loading test cathode (11 mg cm^{-2}). For pouch-type cells, PANI loadings of 8.4 and 16.5 mg cm^{-2} were used (surface area: 5 cm^2). Galvanostatic charge-discharge tests were conducted in a voltage range of 0.5–1.45 V under the specified current density conditions. The galvanostatic intermittent titration technique (GITT) was performed using 0.1 A g^{-1} current density for 1 min charge/discharge followed by 3 min of rest.

Characterization

The HB network of water was analyzed using ATR FTIR (Bruker INVENIO). Changes in the water environment were investigated using ^1H NMR (Bruker AV III 600 MHz). Raman spectroscopy and ^{17}O NMR were used to observe chemical structure changes in DMSO upon Zn salt dissolution. Raman spectra were collected using Horiba Jobin Yvon-Labram Aramis with a 532 nm excitation laser wavelength. Surface morphologies of the Zn electrodes were examined with SEM (Tescan XEIA FEG SEM). The SEI components on the Zn metal surface were analyzed using XPS (Kratos Axis Supra plus) and ToF-SIMS (Tescan S8252X). XRD (Bruker D8 Advance, Cu radiation) was performed to observe the formation of crystalline products on the Zn metal surface after cycling tests. *In situ* H_2 gas evolutions were detected using Hiden HPR-40 DEMS.

Computational method

Calculations were performed using the Material Studio 2023 software package from BIOVIA. Classical molecular dynamics simulations were conducted to examine the electrolyte structure using the RDF through the Forcite module and the COMPASSIII force field (version 1.2). Initial electrolyte configurations were generated by randomly distributing each component based on the concentrations specified in Table S4. The system was equilibrated through a sequential process: (1) geometric optimization with convergence tolerances set at 2 × 10^{-5} kcal mol^{-1} for energy, 1 × 10^{-3} kcal mol^{-1} $Å^{-1}$ for force, and displacement with 1 × 10^{-5} Å; (2) an isothermal-isobaric ensemble (NPT) simulation at standard atmospheric pressure (1.013 × 10^{-4} GPa) and an annealing temperature of 323 K for 2 ns to minimize initial configuration effects; (3) NPT simulation at room temperature (298 K) for 2 ns; (4) canonical (NVT) ensemble simulation at 298 K for 2 ns; and (5) NVT simulation at 298 K for 5 ns. RDF calculations were performed using the equilibrated system from the final protocol step. SA calculations employed a thermodynamic integration method with equilibrated $Zn(TFSI)_2$ electrolytes in each pure solvent (DG, DS, PP, EG, and H_2O).

The solvation structures of Zn ions in each electrolyte from molecular dynamics simulations were used to calculate the electron density variation of H_2O in the Zn ion's 1st solvation shell. Electron density changes were analyzed using density functional theory (DFT) calculations with the $DMol^3$ module. The Perdew-Burke-Ernzerhof generalized gradient approximation (PBE-GGA) functional was used to correlate electron exchange with unrestricted spin polarization. Double numerical plus polarization (DNP+) was used for the basis set. For the DFT calculations, convergence tolerances were set to 1 × 10^{-5} Ha, 2 × 10^{-3} Ha $Å^{-1}$, and 5 × 10^{-3} Å for energy, maximum force, and maximum displacement, respectively.

RESOURCE AVAILABILITY

Lead contact

Requests for further information and resources should be directed to and will be fulfilled by the lead contact, Chunsheng Wang (cswang@umd.edu).

Materials availability

This study did not generate new, unique reagents.

Data and code availability

All data generated and analyzed for the study are presented in the manuscript and supplemental information. Any additional information is available from the lead contact upon request.

ACKNOWLEDGMENTS

This research was supported by the Basic Science Research Program through the National Research Foundation of Korea (NRF) funded by the Ministry of Education (RS-2023-00243176). Also, this work is supported by the Aqueous Battery Consortium, an energy innovation hub under the US Department of Energy, Office of Basic Energy Sciences, Division of Materials Science and Engineering.

AUTHOR CONTRIBUTIONS

J.H. and C.W. conceived the idea of this work and designed experiments. J.H. conducted experiments and computational calculations. D.D. and Z.W. provided discussion. Z.W. conducted an XRD analysis. J.H. wrote the original draft, and J.H. and C.W. revised the manuscript. C.W. directed the project.

DECLARATION OF INTERESTS

The authors declare no competing interests.

SUPPLEMENTAL INFORMATION

Supplemental information can be found online at https://doi.org/10.1016/j.joule.2025.101844.

Received: September 5, 2024
Revised: November 28, 2024
Accepted: January 13, 2025
Published: February 4, 2025

REFERENCES

1. Ma, L., Schroeder, M.A., Borodin, O., Pollard, T.P., Ding, M.S., Wang, C., and Xu, K. (2020). Realizing high zinc reversibility in rechargeable batteries. Nat. Energy *5*, 743–749. https://doi.org/10.1038/s41560-020-0674-x.
2. Jiang, H., Tang, L., Fu, Y., Wang, S., Sandstrom, S.K., Scida, A.M., Li, G., Hoang, D., Hong, J.J., Chiu, N.-C., et al. (2023). Chloride electrolyte enabled practical zinc metal battery with a near-unity Coulombic efficiency. Nat. Sustain. *6*, 806–815. https://doi.org/10.1038/s41893-023-01092-x.
3. Huang, J., Zhong, Y., Fu, H., Zhao, Y., Li, S., Xie, Y., Zhang, H., Lu, B., Chen, L., Liang, S., et al. (2024). Interfacial biomacromolecular engineering toward stable ah-level aqueous zinc batteries. Adv. Mater. *36*, 2406257. https://doi.org/10.1002/adma.202406257.
4. Li, C., Shyamsunder, A., Hoane, A.G., Long, D.M., Kwok, C.Y., Kotula, P.G., Zavadil, K.R., Gewirth, A.A., and Nazar, L.F. (2022). Highly reversible Zn anode with a practical areal capacity enabled by a sustainable electrolyte and superacid interfacial chemistry. Joule *6*, 1103–1120. https://doi.org/10.1016/j.joule.2022.04.017.
5. Zhao, Q., Liu, W., Ni, X., Yu, H., Zhang, C., Wang, B., Jiang, L., He, H., Chen, Y., and Chen, L. (2024). Steering interfacial renovation with highly electronegative Cl modulated trinity effect for exceptional durable zinc anode. Adv. Funct. Mater. *34*, 2404219. https://doi.org/10.1002/adfm.202404219.
6. Wang, Y., Mo, L., Zhang, X., Ren, Y., Wei, T., He, Y., Huang, Y., Zhang, H., Tan, P., Li, Z., et al. (2024). Regulating water activity for all-climate aqueous zinc-ion batteries. Adv. Energy Mater. *14*, 2402041. https://doi.org/10.1002/aenm.202402041.
7. Wang, Y., Wang, Z., Pang, W.K., Lie, W., Yuwono, J.A., Liang, G., Liu, S., Angelo, A.M.D., Deng, J., Fan, Y., et al. (2023). Solvent control of water O−H bonds for highly reversible zinc ion batteries. Nat. Commun. *14*, 2720. https://doi.org/10.1038/s41467-023-38384-x.
8. You, C., Wu, R., Yuan, X., Liu, L., Ye, J., Fu, L., Han, P., and Wu, Y. (2023). An inexpensive electrolyte with double-site hydrogen bonding and a regulated Zn 2+ solvation structure for aqueous Zn-ion batteries capable of high rate and ultra-long low-temperature operation. Energy Environ. Sci. *16*, 5096–5107. https://doi.org/10.1039/D3EE01741A.
9. Wang, R., Ma, Q., Zhang, L., Liu, Z., Wan, J., Mao, J., Li, H., Zhang, S., Hao, J., Zhang, L., et al. (2023). An aqueous electrolyte regulator for highly stable zinc anode under −35 to 65 °C. Adv. Energy Mater. *13*, 1–12. https://doi.org/10.1002/aenm.202302543.
10. Sheng, D., Liu, X., Yang, Z., Zhang, M., Li, Y., Ren, P., Yan, X., Shen, Z.X., and Chao, D. (2024). Hydrogen bond network regulation in electrolyte structure for Zn-based aqueous batteries. Adv. Funct. Mater. *34*, 2402014. https://doi.org/10.1002/adfm.202402014.
11. Zhang, R., Pang, W.K., Vongsvivut, J., Yuwono, J.A., Li, G., Lyu, Y., Fan, Y., Zhao, Y., Zhang, S., Mao, J., et al. (2024). Weakly solvating aqueous-based electrolyte facilitated by a soft co-solvent for extreme temperature operations of zinc-ion batteries. Energy Environ. Sci. *17*, 4569–4581. https://doi.org/10.1039/D4EE00942H.
12. Huang, C., Zhao, X., Hao, Y., Yang, Y., Qian, Y., Chang, G., Zhang, Y., Tang, Q., Hu, A., and Chen, X. (2023). Selection criteria for electrical double layer structure regulators enabling stable Zn metal anodes. Energy Environ. Sci. *16*, 1721–1731. https://doi.org/10.1039/D3EE00045A.
13. Wang, W., Chen, S., Liao, X., Huang, R., Wang, F., Chen, J., Wang, Y., Wang, F., and Wang, H. (2023). Regulating interfacial reaction through electrolyte chemistry enables gradient interphase for low-temperature zinc metal batteries. Nat. Commun. *14*, 5443. https://doi.org/10.1038/s41467-023-41276-9.
14. Zhang, W., Yao, Q., Wang, C., Feng, R., Chen, N., Zhu, J., and Li, Z. (2023). Taming Zn electrochemistry with carbon nitride: atomically gradient interphase for highly reversible aqueous Zn batteries. Adv. Funct. Mater *34*. https://doi.org/10.1002/adfm.202303590.
15. Cao, L., Li, D., Pollard, T., Deng, T., Zhang, B., Yang, C., Chen, L., Vatamanu, J., Hu, E., Hourwitz, M.J., et al. (2021). Fluorinated interphase enables reversible aqueous zinc battery chemistries. Nat. Nanotechnol. *16*, 902–910. https://doi.org/10.1038/s41565-021-00905-4.
16. Li, Y., Yu, Z., Huang, J., Wang, Y., and Xia, Y. (2023). Constructing solid electrolyte interphase for aqueous zinc batteries. Angew. Chem. Int. Ed. Engl. *62*, e202309957. https://doi.org/10.1002/ange.202309957.
17. Tripathi, A.M., Su, W.-N., and Hwang, B.J. (2018). In situ analytical techniques for battery interface analysis. Chem. Soc. Rev. *47*, 736–851. https://doi.org/10.1039/C7CS00180K.
18. Rodrigues, M.-T.F., Sayed, F.N., Gullapalli, H., and Ajayan, P.M. (2018). High-temperature solid electrolyte interphases (SEI) in graphite electrodes. J. Power Sources *381*, 107–115. https://doi.org/10.1016/j.jpowsour.2018.01.070.
19. Reichardt, C. (1994). Solvatochromic dyes as solvent polarity indicators. Chem. Rev. *94*, 2319–2358. https://doi.org/10.1021/cr00032a005.
20. Gupta, R., Rayeeny, S.A., Das, S.S., and Bhargava, H.N. (1995). A comparative study of the catalytic action of water-miscible organic solvents on the hydrolytic degradation of long-chain polyphosphates. Polym. Degrad. Stab. *50*, 183–188. https://doi.org/10.1016/0141-3910(95)00144-1.
21. Su, C.-C., He, M., Amine, R., Rojas, T., Cheng, L., Ngo, A.T., and Amine, K. (2019). Solvating power series of electrolyte solvents for lithium batteries. Energy Environ. Sci. *12*, 1249–1254. https://doi.org/10.1039/C9EE00141G.
22. Barnes, P., Finney, J.L., Nicholas, J.D., and Quinn, J.E. (1979). Cooperative effects in simulated water. Nature *282*, 459–464. https://doi.org/10.1038/282459a0.

23. Gutmann, V. (1976). Empirical parameters for donor and acceptor properties of solvents. Electrochim. Acta *21*, 661–670. https://doi.org/10.1016/0013-4686(76)85034-7.

24. Stangret, J. (2002). Donor properties of water in organic solvents derived from infrared spectra of HDO. J. Mol. Struct. *643*, 29–35. https://doi.org/10.1016/S0022-2860(02)00315-0.

25. Marcus, Y. (1992). The effectivity of solvents as hydrogen bond donors. J. Solut. Chem. *21*, 1289. https://doi.org/10.1007/BF00667223.

26. Huang, Z., Li, Z., Wang, Y., Cong, J., Wu, X., Song, X., Ma, Y., Xiang, H., and Huang, Y. (2023). Regulating Zn(002) deposition toward long cycle life for Zn metal batteries. ACS Energy Lett. *8*, 372–380. https://doi.org/10.1021/acsenergylett.2c02359.

27. Ortega, J., Ràfols, C., Bosch, E., and Rosés, M. (1996). Solute–solvent and solvent–solvent interactions in binary solvent mixtures. Part 3. The E T (30) polarity of binary mixtures of hydroxylic solvents. J. Chem. Soc. Perkin Trans. *2*, 1497–1503. https://doi.org/10.1039/P29960001497.

28. Stroka, J., Herfort, I., and Schneider, H. (1990). Dimethylpropyleneurea-water mixtures: 1. Physical properties. J. Solut. Chem. *19*, 743–753. https://doi.org/10.1007/BF00647101.

29. Gojło, E., Gampe, T., Krakowiak, J., and Stangret, J. (2007). Hydration of aprotic donor solvents studied by means of FTIR spectroscopy. J. Phys. Chem. A *111*, 1827–1834. https://doi.org/10.1021/jp065599p.

30. Jóźwiak, M., Szylberg, M., Piekarski, H., Kustrzepa, K., and Jóźwiak, A. (2017). Effect of properties of the N,N -dimethylformamide–methanol and N,N -dimethylformamide–water mixtures on the solution enthalpy of glymes in these mixtures at 298.15 K. Thermochim. Acta *652*, 53–61. https://doi.org/10.1016/j.tca.2017.03.001.

31. Gejji, S.P., Suresh, C.H., Babu, K., and Gadre, S.R. (1999). Ab initio structure and vibrational frequencies of (CF 3 SO 2) 2 N - Li + ion pairs. J. Phys. Chem. A *103*, 7474–7480. https://doi.org/10.1021/jp984474k.

32. Feng, D., Cao, F., Hou, L., Li, T., Jiao, Y., and Wu, P. (2021). Immunizing aqueous Zn batteries against dendrite formation and side reactions at various temperatures via electrolyte additives. Small *17*, e2103195. https://doi.org/10.1002/smll.202103195.

33. Krishnamoorthy, A.N., Zeman, J., Holm, C., and Smiatek, J. (2016). Preferential solvation and ion association properties in aqueous dimethyl sulfoxide solutions. Phys. Chem. Chem. Phys. *18*, 31312–31322. https://doi.org/10.1039/C6CP05909K.

34. Balk, R.W., and Somsen, G. (1985). Preferential solvation and hydrophobic hydration of polyols in mixtures of water and N,N-dimethylformamide. J. Phys. Chem. *89*, 5093–5097. https://doi.org/10.1021/j100269a041.

35. Yi, X., Fu, H., Rao, A.M., Zhang, Y., Zhou, J., Wang, C., and Lu, B. (2024). Safe electrolyte for long-cycling alkali-ion batteries. Nat. Sustain. *7*, 326–337. https://doi.org/10.1038/s41893-024-01275-0.

36. Yoon, G., Kim, H., Park, I., and Kang, K. (2017). Conditions for reversible Na intercalation in graphite: theoretical studies on the interplay among guest ions, solvent, and graphite Host. Adv. Energy Mater. *7*, 1601519. https://doi.org/10.1002/aenm.201601519.

37. Yang, C., Xia, J., Cui, C., Pollard, T.P., Vatamanu, J., Faraone, A., Dura, J.A., Tyagi, M., Kattan, A., Thimsen, E., et al. (2023). All-temperature zinc batteries with high-entropy aqueous electrolyte. Nat. Sustain. *6*, 325–335. https://doi.org/10.1038/s41893-022-01028-x.

38. Heo, J., Roh, Y., Shin, K., Lee, C., Wang, C., and Kim, H.-T. (2024). Versatile Zn hosting Lewis-basic interfacial layer for high-performant Zn reversibility in aqueous Zn ion battery. Energy Storage Mater. *71*, 103580. https://doi.org/10.1016/j.ensm.2024.103580.

39. Zhao, H., Wang, J., Shao, H., Xu, K., and Deng, Y. (2022). Gas generation mechanism in Li-metal batteries. Energy Environ. Materials *5*, 327–336. https://doi.org/10.1002/eem2.12180.

40. Kim, S., Kim, H.S., Kim, B., Kim, Y.J., Jung, J.W., and Ryu, W.H. (2023). In situ gas analysis by differential electrochemical mass spectrometry for advanced rechargeable batteries: a review. Adv. Energy Mater. *13*, 1–33. https://doi.org/10.1002/aenm.202301983.

41. Bonet, F. (1999). Electrochemical reduction of noble metal species in ethylene glycol at platinum and glassy carbon rotating disk electrodes. Solid State Ionics *126*, 337–348. https://doi.org/10.1016/S0167-2738(99)00240-4.

42. Reichardt, C. (1979). Empirical parameters of solvent polarity as linear free-energy relationships. Angew. Chem. Int. Ed. Engl. *18*, 98–110. https://doi.org/10.1002/anie.197900981.

43. Chen, R., Zhang, W., Guan, C., Zhou, Y., Gilmore, I., Tang, H., Zhang, Z., Dong, H., Dai, Y., Du, Z., et al. (2024). Rational design of an in-situ polymer-inorganic hybrid solid electrolyte interphase for realising stable Zn metal anode under harsh conditions. Angew. Chem. Int. Ed. Engl. *63*, e202401987. https://doi.org/10.1002/ange.202401987.

44. Xia, S., Luo, Q., Liu, J., Yang, X., Lei, J., Shao, J., and Tang, X. (2024). In situ spontaneous construction of zinc phosphate coating layer toward highly reversible zinc metal anodes. Small *20*, e2310497. https://doi.org/10.1002/smll.202310497.

45. Hu, N., Lv, W., Chen, W., Tang, H., Zhang, X., Qin, H., Huang, D., Zhu, J., Chen, Z., Xu, J., et al. (2024). A double-charged organic molecule additive to customize electric double layer for super-stable and deep-rechargeable Zn metal pouch batteries. Adv. Funct. Mater. *34*, 1–13. https://doi.org/10.1002/adfm.202311773.

46. Zheng, J., Deng, Y., Li, W., Yin, J., West, P.J., Tang, T., Tong, X., Bock, D.C., Jin, S., Zhao, Q., et al. (2022). Design principles for heterointerfacial alloying kinetics at metallic anodes in rechargeable batteries. Sci. Adv. *8*, eabq6321. https://doi.org/10.1126/sciadv.abq6321.

47. Han, J., Euchner, H., Kuenzel, M., Hosseini, S.M., Groß, A., Varzi, A., and Passerini, S. (2021). A thin and uniform fluoride-based artificial interphase for the zinc metal anode enabling reversible Zn/MnO 2 batteries. ACS Energy Lett. *6*, 3063–3071. https://doi.org/10.1021/acsenergylett.1c01249.

48. Hao, J., Li, B., Li, X., Zeng, X., Zhang, S., Yang, F., Liu, S., Li, D., Wu, C., and Guo, Z. (2020). An in-depth study of Zn metal surface chemistry for advanced aqueous Zn-ion batteries. Adv. Mater. *32*, e2003021. https://doi.org/10.1002/adma.202003021.

49. Nayak, P.K., Wang, Z., Anjum, D.H., Hedhili, M.N., and Alshareef, H.N. (2015). Highly stable thin film transistors using multilayer channel structure. Appl. Phys. Lett. *106*, 103505. https://doi.org/10.1063/1.4914971.

50. Xiong, X., Wang, Y., Ma, J., He, Y., Huang, J., Feng, Y., Ban, C., Gan, L.-Y., and Zhou, X. (2023). Oxygen vacancy engineering of zinc oxide for boosting piezo-electrocatalytic hydrogen evolution. Appl. Surf. Sci. *616*, 156556. https://doi.org/10.1016/j.apsusc.2023.156556.

51. Sofianos, V.M., Lee, J., Silvester, D.S., Samanta, P.K., Paskevicius, M., English, N.J., and Buckley, C.E. (2021). Diverse morphologies of zinc oxide nanoparticles and their electrocatalytic performance in hydrogen production. J. Energy Chem. *56*, 162–170. https://doi.org/10.1016/j.jechem.2020.07.051.

52. Zhao, Z., Zhao, J., Hu, Z., Li, J., Li, J., Zhang, Y., Wang, C., and Cui, G. (2019). Long-life and deeply rechargeable aqueous Zn anodes enabled by a multifunctional brightener-inspired interphase. Energy Environ. Sci. *12*, 1938–1949. https://doi.org/10.1039/C9EE00596J.

53. Wang, Y., Wang, T., Bu, S., Zhu, J., Wang, Y., Zhang, R., Hong, H., Zhang, W., Fan, J., and Zhi, C. (2023). Sulfolane-containing aqueous electrolyte solutions for producing efficient ampere-hour-level zinc metal battery pouch cells. Nat. Commun. *14*, 1828. https://doi.org/10.1038/s41467-023-37524-7.

54. Wang, Y., Liang, B., Zhu, J., Li, G., Li, Q., Ye, R., Fan, J., and Zhi, C. (2023). Manipulating electric double layer adsorption for stable solid-electrolyte interphase in 2.3 ah Zn-pouch cells. Angew. Chem. Int. Ed. Engl. *62*, e202302583. https://doi.org/10.1002/anie.202302583.

55. Chen, Z., Yang, Q., Mo, F., Li, N., Liang, G., Li, X., Huang, Z., Wang, D., Huang, W., Fan, J., et al. (2020). Aqueous zinc–tellurium batteries with ultraflat discharge plateau and high volumetric capacity. Adv. Mater. *32*, e2001469. https://doi.org/10.1002/adma.202001469.

56. Tian, C., Wang, H., Xie, L., Zhong, Y., and Hu, Y. (2024). Arrays of hierarchical Zincophilic nanorods with trapping-and-leveling deposition for ultrastable Zn metal anodes. Adv. Energy Mater. *14*, 1–13. https://doi.org/10.1002/aenm.202400276.

57. Li, X., Xie, X., Lv, R., Na, B., Wang, B., and He, Y. (2019). Nanostructured polypyrrole composite aerogels for a rechargeable flexible aqueous Zn-ion battery with high rate capabilities. Energy Technol. *7*, 1–6. https://doi.org/10.1002/ente.201801092.

58. Chen, Y., Dai, H., Fan, K., Zhang, G., Tang, M., Gao, Y., Zhang, C., Guan, L., Mao, M., Liu, H., et al. (2023). A recyclable and scalable high-capacity organic battery. Angew. Chem. *135*, 1–8. https://doi.org/10.1002/ange.202302539.

59. Zhang, Q., Ma, Y., Lu, Y., Li, L., Wan, F., Zhang, K., and Chen, J. (2020). Modulating electrolyte structure for ultralow temperature aqueous zinc batteries. Nat. Commun. *11*, 4463. https://doi.org/10.1038/s41467-020-18284-0.

60. Ma, G., Miao, L., Dong, Y., Yuan, W., Nie, X., Di, S., Wang, Y., Wang, L., and Zhang, N. (2022). Reshaping the electrolyte structure and interface chemistry for stable aqueous zinc batteries. Energy Storage Mater. *47*, 203–210. https://doi.org/10.1016/j.ensm.2022.02.019.

61. Li, W., Wang, K., Zhou, M., Zhan, H., Cheng, S., and Jiang, K. (2018). Advanced low-cost, high-voltage, long-life aqueous hybrid sodium/zinc batteries enabled by a dendrite-free zinc anode and concentrated electrolyte. ACS Appl. Mater. Interfaces *10*, 22059–22066. https://doi.org/10.1021/acsami.8b04085.

62. Yuan, W., Nie, X., Wang, Y., Li, X., Ma, G., Wang, Y., Shen, S., and Zhang, N. (2023). Orientational electrodeposition of highly (002)-textured zinc metal anodes enabled by iodide ions for stable aqueous zinc batteries. ACS Nano *17*, 23861–23871. https://doi.org/10.1021/acsnano.3c08095.

63. Dong, J., Su, L., Peng, H., Wang, D., Zong, H., Wang, G., and Yang, J. (2024). Spontaneous molecule aggregation for nearly single-ion conducting sol electrolyte to advance aqueous zinc metal batteries: the case of tetraphenylporphyrin. Angew. Chem. Int. Ed. Engl. *63*, e202401441. https://doi.org/10.1002/anie.202401441.